

Probing the polarized emission from SMC X-1: the brightest X-ray pulsar observed by IXPE

Sofia V. Forsblom¹, Sergey S. Tsygankov¹, Juri Poutanen¹, Victor Doroshenko², Alexander A. Mushtukov³, Mason Ng⁴, Swati Ravi⁴, Herman L. Marshall⁴, Alessandro Di Marco⁵, Fabio La Monaca^{5,6,7}, Christian Malacaria⁸, Guglielmo Mastroserio⁹, Vladislav Loktev¹, Andrea Possenti¹⁰, Valery F. Suleimanov², Roberto Taverna¹¹, Iván Agudo¹², Lucio A. Antonelli^{13,14}, Matteo Bachetti¹⁰, Luca Baldini^{15,16}, Wayne H. Baumgartner¹⁷, Ronaldo Bellazzini¹⁵, Stefano Bianchi¹⁸, Stephen D. Bongiorno¹⁷, Raffaella Bonino^{19,20}, Alessandro Brez¹⁵, Niccolò Bucciantini^{21,22,23}, Fiamma Capitanio⁵, Simone Castellano¹⁵, Elisabetta Cavazzuti²⁴, Chien-Ting Chen²⁵, Stefano Ciprini^{26,14}, Enrico Costa⁵, Alessandra De Rosa⁵, Ettore Del Monte⁵, Laura Di Gesu²⁴, Niccolò Di Lalla²⁷, Immacolata Donnarumma²⁴, Michal Dovčiak²⁸, Steven R. Ehlert¹⁷, Teruaki Enoto²⁹, Yuri Evangelista⁵, Sergio Fabiani⁵, Riccardo Ferrazzoli⁵, Javier A. Garcia³⁰, Shuichi Gunji³¹, Kiyoshi Hayashida^{32*}, Jeremy Heyl³³, Wataru Iwakiri³⁴, Svetlana G. Jorstad^{35,36}, Philip Kaaret¹⁷, Vladimir Karas²⁸, Fabian Kislak³⁷, Takao Kitaguchi²⁹, Jeffery J. Kolodziejczak¹⁷, Henric Krawczynski³⁸, Luca Latronico¹⁹, Ioannis Liodakis^{17,39}, Simone Maldera¹⁹, Alberto Manfreda⁴⁰, Frédéric Marin⁴¹, Andrea Marinucci²⁴, Alan P. Marscher³⁵, Francesco Massaro^{19,20}, Giorgio Matt¹⁸, Ikuyuki Mitsuishi⁴², Tsunefumi Mizuno⁴³, Fabio Muleri⁵, Michela Negro⁴⁴, Chi-Yung Ng⁴⁵, Stephen L. O’Dell¹⁷, Nicola Omodei²⁷, Chiara Oppedisano¹⁹, Alessandro Papitto¹³, George G. Pavlov⁴⁶, Abel L. Peirson²⁷, Matteo Perri^{14,13}, Melissa Pesce-Rollins¹⁵, Pierre-Olivier Petrucci⁴⁷, Maura Pilia¹⁰, Simonetta Puccetti¹⁴, Brian D. Ramsey¹⁷, John Rankin⁵, Ajay Ratheesh⁵, Oliver J. Roberts²⁵, Roger W. Romani²⁷, Carmelo Sgrò¹⁵, Patrick Slane⁴⁸, Paolo Soffitta⁵, Gloria Spandre¹⁵, Douglas A. Swartz²⁵, Toru Tamagawa²⁹, Fabrizio Tavecchio⁴⁹, Yuzuru Tawara⁴², Allyn F. Tennant¹⁷, Nicholas E. Thomas¹⁷, Francesco Tombesi^{6,26}, Alessio Trois¹⁰, Roberto Turolla^{11,50}, Jacco Vink⁵¹, Martin C. Weisskopf¹⁷, Kinwah Wu⁵⁰, Fei Xie^{52,5}, and Silvia Zane⁵⁰

(Affiliations can be found after the references)

2024

ABSTRACT

Recent observations of X-ray pulsars (XRP) performed by the Imaging X-ray Polarimetry Explorer (IXPE) have made it possible to investigate the intricate details of these objects in a new way, thanks to the added value of X-ray polarimetry. Here we present the results of the IXPE observations of SMC X-1, a member of the small group of XRP displaying super-orbital variability. SMC X-1 was observed by IXPE three separate times during the high state of its super-orbital period. The observed luminosity in the 2–8 keV energy band of $L \sim 2 \times 10^{38}$ erg s⁻¹ makes SMC X-1 the brightest XRP ever observed by IXPE. We detect significant polarization in all three observations, with values of the phase-averaged polarization degree (PD) and polarization angle (PA) of $3.2 \pm 0.8\%$ and $97^\circ \pm 8^\circ$ for Observation 1, $3.0 \pm 0.9\%$ and $90^\circ \pm 8^\circ$ for Observation 2, and $5.5 \pm 1.1\%$ and $80^\circ \pm 6^\circ$ for Observation 3, for the spectro-polarimetric analysis. The observed PD shows an increase over time with decreasing luminosity, while the PA decreases in decrements of $\sim 10^\circ$. The phase-resolved spectro-polarimetric analysis reveals significant detection of polarization in three out of seven phase bins, with the PD ranging between $\sim 2\%$ and $\sim 10\%$, and a corresponding range in the PA from $\sim 70^\circ$ to $\sim 100^\circ$. The pulse-phase resolved PD displays an apparent anti-correlation with the flux. Using the rotating vector model, we obtain constraints on the pulsar’s geometrical properties for the individual observations. The position angle of the pulsar displays an evolution over time supporting the idea that we observe changes related to different super-orbital phases. Scattering in the wind of the precessing accretion disk may be responsible for the behavior of the polarimetric properties observed during the high-state of SMC X-1’s super-orbital period.

Key words. accretion, accretion disks – magnetic fields – polarization – pulsars: individual: SMC X-1 – stars: neutron – X-rays: binaries

1. Introduction

High-mass X-ray Binaries (HMXBs) involve a compact object accreting matter from a massive companion star. For strongly magnetized neutron stars (NSs), the accretion flow is disrupted by the magnetosphere at a distance of the order of $10^8 - 10^9$ cm. The matter follows then the magnetic field lines onto the NSs

surface, where the gravitational potential energy of the accreted matter is released. Depending on the accretion rate, either hot spots or extended accretion columns may form at the magnetic poles. The misalignment between the magnetic poles and spin axis leads to pulsed X-ray emission, and the appearance of an X-ray pulsar (XRP; for a recent review, see, e.g., [Mushtukov & Tsygankov 2024](#)). The observed properties and phase-dependence of the pulsed X-ray emission are defined by the

* Deceased.

emission region geometry, the pulsar’s orientation with respect to the observer, and details of radiative transfer in the strong magnetic field. There are, however, no robust theoretical models capable of describing those comprehensively. One of the main issues is the uncertainty in the basic geometry of XRP. Polarimetric observations can be used to determine the pulsar geometry (e.g., the inclination of the pulsar spin to the line of sight and the magnetic obliquity) and possibly to distinguish the emission region geometry.

The immense magnetic field of the NS and its impact on Compton scattering cross-sections are the main reasons for the polarized X-ray emission from XRPs. The scattering of photons in highly magnetized plasma is expected to result in a large degree of polarization (up to 80%) of the emerging X-ray emission for favorable orientations. It has been shown (Meszaros et al. 1988) that the linear X-ray polarization is strongly dependent on the geometry of the emission region and variable with energy and pulse phase, and phase-resolved polarimetry can be used to constrain the viewing geometry and discern different radiation models. IXPE has made it possible to detect the linear X-ray polarization for several tens of astrophysical X-ray sources including XRPs: Her X-1 (Doroshenko et al. 2022; Heyl et al. 2024; Zhao et al. 2024), Cen X-3 (Tsygankov et al. 2022), X Persei (Mushtukov et al. 2023), 4U 1626–67 (Marshall et al. 2022), Vela X-1 (Forsblom et al. 2023), GRO J1008–57 (Tsygankov et al. 2023), EXO 2030+375 (Malacaria et al. 2023), LS V +44 17 (Doroshenko et al. 2023), GX 301–2 (Suleimanov et al. 2023), and Swift J0243.6+6124 (Poutanen et al. 2024). The geometry of the emission region depends on the accretion luminosity, and two main emission region geometries can be distinguished based on the local mass accretion rate: a hot spot and an accretion column. The critical luminosity separating these two accretion regimes is a function of the physical and geometrical parameters of the system. The XRPs observed by IXPE so far have all been in the sub-critical regime, making observations of super-critical XRPs important objects to supplement the information of the polarization properties of XRPs in general. Polarimetric observations of the bright XRP SMC X-1 can help provide information on the super-critical regime and shed light on the effects of accretion columns on the observed polarization.

SMC X-1, a well-studied HMXB in the Small Magellanic Cloud, was initially detected by Price et al. (1971) and later confirmed as a discrete source by Leong et al. (1971), who observed significant variability in the intensity and spectrum. Schreier et al. (1972) verified its binary nature, discovering periodic occultations with a ~ 3.9 d orbital period and measuring the binary orbit inclination of $\sim 70^\circ$. SMC X-1 also exhibits pulsations with the period of about 0.7 s, with varying pulse characteristics over time (Lucke et al. 1976). SMC X-1, one of a few super-giant X-ray binaries known for Roche lobe overflow accretion, consistently emits near or above its Eddington luminosity, which is around 1.3×10^{38} erg s $^{-1}$ for an estimated mass of $1.1M_\odot$ for the NS in the system (van der Meer et al. 2007). Its apparent luminosity varies between approximately 10^{37} erg s $^{-1}$ in the low state to over 5×10^{38} erg s $^{-1}$ in the high state, more than three times its Eddington luminosity (Bonnet-Bidaud & van der Klis 1981). In addition to this persistent emission, SMC X-1 also displays type II X-ray bursts lasting tens of seconds (Angelini et al. 1991; Rai et al. 2018). The near- to super-Eddington luminosity places SMC X-1 between less luminous Be/X-ray binaries (Reig 2011) and brighter ultra-luminous XRPs (Kaaret et al. 2017).

SMC X-1 is also part of an important, but small, group of XRPs that display super-orbital variability, believed to be caused by a warped and precessing accretion disk. The precession of the

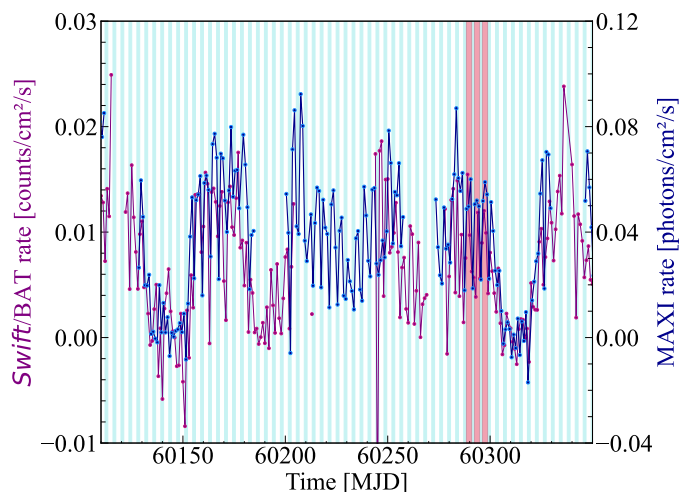


Fig. 1. *Swift*/BAT (15–50 keV) and MAXI (4–10 keV) one-day averaged light curves of SMC X-1 in purple and blue, respectively. Vertical light blue lines show the eclipses and vertical pink lines display the times of the observations with IXPE. Error bars have been removed for visual clarity.

disk causes periodic, partial obscuration of the central source, giving rise to the modulation of the X-ray flux at the precession period. The super-orbital period of SMC X-1 is not steady, as noted by Wojdowski et al. (1998). An instability in the warped accretion disk, changing its geometry as it cycles between stable modes, is believed to cause so-called “excursions”, during which the super-orbital period decreases from its average value of 55 d to ~ 40 d (Clarkson et al. 2003; Dage et al. 2019; Hu et al. 2013). The precession of the disk in SMC X-1 gives rise to three distinct super-orbital states: the high-state characterized by maximum source flux, the low-state of minimum flux (caused by the occultation of the NS by the disk), and the intermediate state marking the transition between the high and low state. SMC X-1 represents a special case where the geometry of the large-scale accretion flow is interconnected with the emission region of the XRP in the very vicinity of the NS. X-ray polarimetry allows probing the emission geometry, and hence, is the perfect tool to study the coupling between the accretion disk and the NS.

2. Observations and data reduction

IXPE is an observatory launched in December 2021 as a NASA/ASI mission (Weisskopf et al. 2022), with the goal of providing imaging polarimetry over the 2–8 keV energy range. IXPE is made up of three grazing incidence telescopes, each consisting of a mirror module assembly (MMA), which focuses X-rays onto a focal-plane polarization-sensitive gas pixel detector unit (DU; Soffitta et al. 2021; Baldini et al. 2021). In addition to measuring the sky coordinates, time of arrival, and energy of each detected photon, it also measures the direction of the photoelectron which allows for polarimetric analysis.

IXPE observed SMC X-1 in December 2023, during the high-state of the super-orbital period (during three consecutive orbital periods, see Fig. 1), for a total exposure of ~ 320 ks. The light curve in the 2–8 keV energy range from the IXPE observations of SMC X-1 is shown in Fig. 2. Three observations (hereinafter referred to as Obs. 1, 2, and 3) occurred between December 10–11, 14–16, and 19–20, with total effective exposures of 111, 110, and 97 ks, respectively. Data have been processed with the IXPEOBSIM package version 31.0.1 using the CalDB released

Table 1. Timing parameters used for Obs. 1, 2, and 3 of SMC X-1.

Parameter	Unit	Obs. 1	Obs. 2	Obs. 3
Epoch	MET ^(a)	218971574.938	219358107.288	219744614.375
Spin period	ms	696.6750±0.0003	696.6712±0.0003	696.6659±0.0004
Spin period derivative	10 ⁻¹¹ s s ⁻¹	-1.3 ± 0.4	-2.9 ± 0.4	-3.0 ± 1.0

Notes. The timing solutions refer to the individual observations. ^(a) IXPE MET (Mission Elapsed Time, in seconds) is equal to $T_{\text{MET}} = (T_{\text{MJD}} - T_{\text{ref}}) \times 86400$, where $T_{\text{ref}} = 57754.00080074074$. The reported epochs define the zero phases of the pulse profiles in Fig. 3.

Table 2. Measurements of the normalized Stokes parameters q and u , PD, and PA for the phase-averaged data of SMC X-1 for different intervals using the pcube algorithm.

Interval	q (%)	u (%)	PD (%)	PA (deg)
Obs. 1	-2.4 ± 1.2	-1.0 ± 1.2	2.6 ± 1.2	101 ± 13
Obs. 2	-3.6 ± 1.2	0.2 ± 1.2	3.6 ± 1.2	88 ± 10
Obs. 3 (incl. dip)	-5.1 ± 1.4	1.8 ± 1.4	5.5 ± 1.4	80 ± 7
Obs. 3 (excl. dip)	-6.3 ± 1.5	2.1 ± 1.5	6.6 ± 1.5	81 ± 6
Obs. 1–3 (incl. dip)	-3.6 ± 0.7	0.2 ± 0.7	3.6 ± 0.7	88 ± 6
Obs. 1–3 (excl. dip)	-3.8 ± 0.7	0.2 ± 0.7	3.8 ± 0.7	89 ± 6
Pre-eclipse dip	0.3 ± 3.8	0.3 ± 3.8	0.4 ± 3.8	unconstrained ^(a)

Notes. ^(a) Formal value for the PA is $20^\circ \pm 250^\circ$.

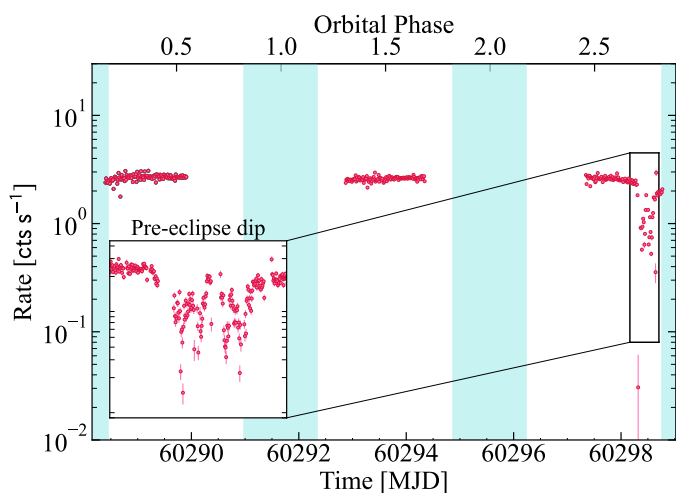


Fig. 2. Light curve of SMC X-1 observed with IXPE in the 2–8 keV energy band. Times of eclipses are shown in the blue shaded regions. The inset displays a higher time-resolution light curve of the pre-eclipse dip detected during the third observation.

on 2024 February 28. The position offset correction and energy calibration were applied before the data analysis. Source photons were extracted from a circular region centered on the source, with the radius $R_{\text{src}} = 80''$. Due to the brightness of the source, background subtraction was not applied and the unweighted approach was used (Di Marco et al. 2022, 2023).

Event arrival times were corrected to the barycenter of the solar system using the `barycorr` tool from the `FTOOLS` package. To account for the effects of binary orbital motion, we corrected observed event arrival times using the ephemerides by Raichur & Paul (2010) and Hu et al. (2019) extrapolated to the IXPE epoch. In particular, the latter is used to estimate the IXPE epoch for mean longitude of 90° , which is estimated at MJD 60287.8042(2) considering reported uncertainties for the zero

epoch, the orbital period, and its derivative. We found, however, that even after correction, the full set of IXPE observations containing three orbital cycles could not be described with a single polynomial timing solution, i.e. some residuals were observed in pulse arrival times, hence the spin evolution of the source is more complex. Considering the presence of gaps in the data, describing that properly is challenging, so we opted to search for the spin period and its derivative using Z^2 statistics in each of the IXPE segments separately, further refining the results using phase-connection. The values for spin period, its derivative, and the pulse epoch for each segment are given in Table 1. This approach allows us to obtain high-quality timing solutions with no phase drifts for each segment as illustrated in Fig. 3.

Stokes I , Q , and U spectra have been re-binned to have at least 30 counts per energy channel, with the same energy-binning applied to all energy spectra. The energy spectra were fitted simultaneously using the `xSPEC` package (version 12.14.0) (Arnaud 1996) using χ^2 statistics and the version 13 instrument response functions (`ixpe:obssim20230702:v13`). The reported uncertainties are at the 68.3% confidence level (1σ) unless stated otherwise.

3. Results

3.1. Light curve and pulse profile

SMC X-1 was observed three separate times during 2023 December 10–20, corresponding to the high-state of the super-orbital period as seen in the light curve (see Fig. 1) obtained by the *Swift*/BAT¹ (Gehrels et al. 2004) monitor and MAXI.² During the third observation, a pre-eclipse dip can be seen in the IXPE light curve (see Fig. 2), as previously observed for SMC X-1 during similar orbital phases (Moon et al. 2003; Trowbridge et al. 2007; Hu et al. 2013). The spin period and spin period derivative were measured for each observation separately

¹ <https://swift.gsfc.nasa.gov/results/transients/>

² <http://maxi.riken.jp/>

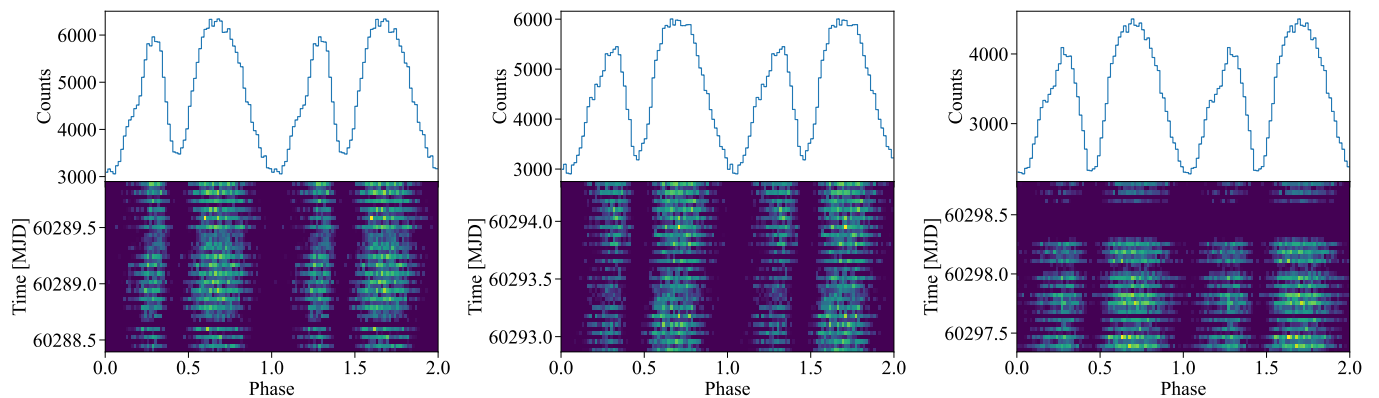


Fig. 3. Phase-aligned pulse profiles and phaseograms for SMC X-1 as seen by IXPE in the 2–8 keV energy band for the Obs. 1 (*left*), Obs. 2 (*center*), and Obs. 3 (*right*).

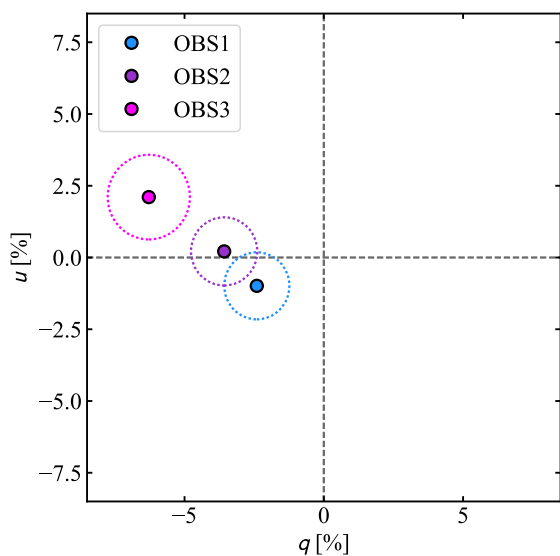


Fig. 4. Phase-averaged normalized Stokes q and u of Observations 1, 2, and 3 (excluding dip) for each separate observation (combining the DUs) for the entire 2–8 keV energy band. The size of the circles correspond to the uncertainty at 68% confidence level.

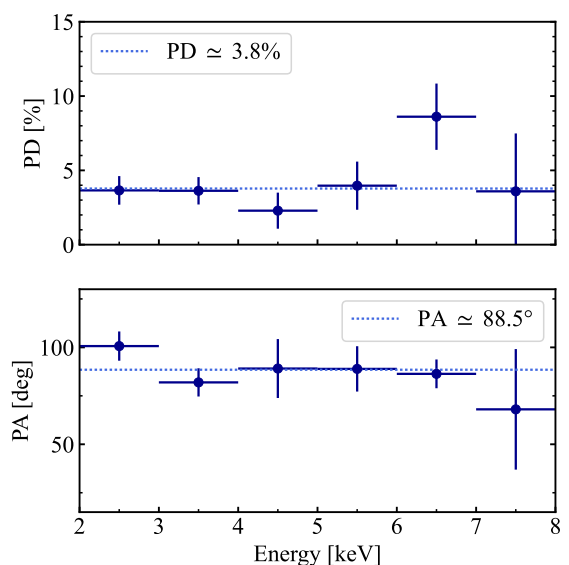


Fig. 5. Energy dependence of the PD and PA for the combined data set (excluding dip), obtained with the *pcube* algorithm.

Table 3. Measurements of the normalized Stokes parameters q and u , PD, and PA in different energy bins using the *pcube* algorithm.

Energy (keV)	q (%)	u (%)	PD (%)	PA (deg)
2–3	-3.4 ± 1.0	-1.3 ± 1.0	3.7 ± 1.0	101 ± 8
3–4	-3.5 ± 0.9	1.0 ± 0.9	3.6 ± 0.9	82 ± 7
4–5	-2.3 ± 1.2	0.1 ± 1.2	2.3 ± 1.2	89 ± 15
5–6	-4.0 ± 1.6	0.2 ± 1.6	4.0 ± 1.6	89 ± 12
6–7	-8.5 ± 2.2	1.1 ± 2.2	8.6 ± 2.2	86 ± 7
7–8	-2.6 ± 3.9	2.5 ± 3.9	3.6 ± 3.9	68 ± 31
2–8	-3.8 ± 0.7	0.2 ± 0.7	3.8 ± 0.7	89 ± 6

and the determined values can be found in Table 1. The resulting pulse profiles for the observations of SMC X-1 in the 2–8 keV energy band are shown in Fig. 3, together with the phaseograms which display the evolution of the pulse profile over the time of each observation.

3.2. Polarimetric analysis

The initial polarimetric analysis of SMC X-1 was carried out using the *xpbin* tool’s *pcube* algorithm included in the *IXPEOBS-SIM* package, which has been implemented according to the formalism by Kislak et al. (2015). Using the unweighted analysis, we compute the normalized Stokes $q = Q/I$ and $u = U/I$ parameters and the PD using the equation $PD = \sqrt{q^2 + u^2}$, and the $PA = \frac{1}{2} \arctan(u/q)$, with the PA measured from north to east counterclockwise on the sky.

The phase-averaged PD and PA in the full 2–8 keV IXPE energy range for Obs. 1–3 are given in Table 2 and shown in Fig. 4. We do not detect polarization during the pre-eclipse dip, with a phase-averaged PD of $0.4 \pm 3.8\%$ and an unconstrained PA. The pre-eclipse data is removed from all subsequent analysis. The PD and PA shows an apparent trend in their behavior over time. The PD appears to be increasing with time, while the PA decreases (in decrements of $\sim 10^\circ$).

In order to increase the statistics of the polarimetric analysis, we combined the data from all three observations using the following steps. First, we created pulse profiles according to the spin period evolution parameters determined for each observa-

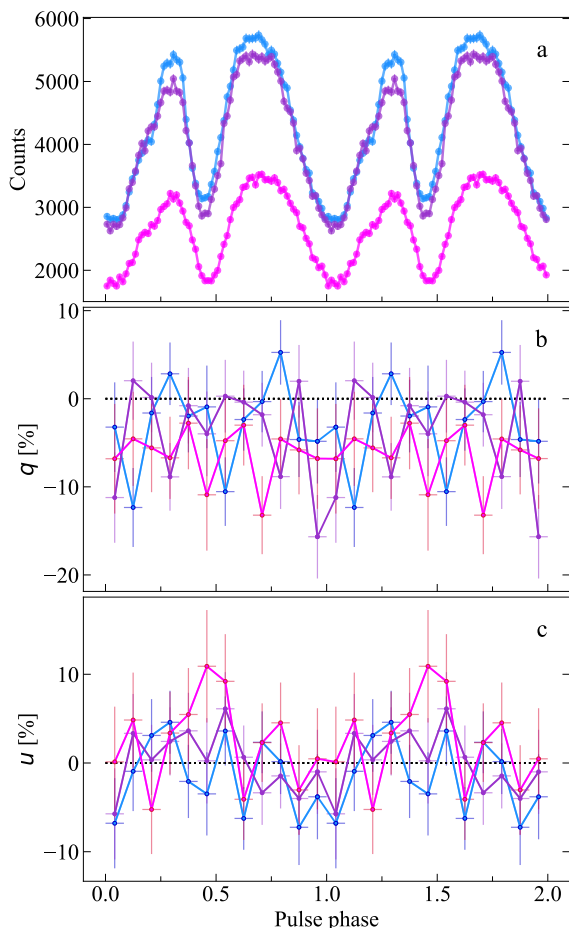


Fig. 6. Phase dependence of the flux and normalized Stokes parameters. Panel (a): pulse profiles during three observations. The normalized Stokes parameters q and u are shown in panels (b) and (c), respectively. The polarimetric analysis was done using `pcube` for three DUs combined in the full 2–8 keV energy band and uniform phase-binning. Observations 1, 2, and 3 are shown in blue, purple, and pink, respectively.

tion separately (see Table 1). The pulse profiles were then cross-correlated to determine the relative phase-shifts between the observations, allowing us to correctly connect the phases. Finally, each event was phase-tagged and the data from the three observations were added, producing a combined data set (excluding pre-eclipse data). The phase-averaged PD and PA for the combined set of observations of SMC X-1 measured in the entire IXPE energy band of 2–8 keV are $3.8 \pm 0.7\%$ and $89^\circ \pm 6^\circ$, respectively.

Next, we studied the energy dependence of the polarization properties of SMC X-1 by performing an energy-resolved polarimetric analysis on the combined data set, dividing the data into six energy bins. The results are given in Table 3 and shown in Fig. 5. No significant energy dependence of the polarization properties is detected. Similarly, we see no energy dependence of the polarimetric properties during the separate observations.

Considering the importance of the variations of PD and PA over the pulsar’s spin phase, next, we performed a phase-resolved polarimetric analysis of the separate observations by splitting the data into 12 uniform phase bins and using the `pcube` algorithm to determine the polarimetric properties of each bin. However, due to poor statistics, we do not detect significant polarization in any phase bin of the separate observations. We do, however, see an indication of different behavior of the normal-

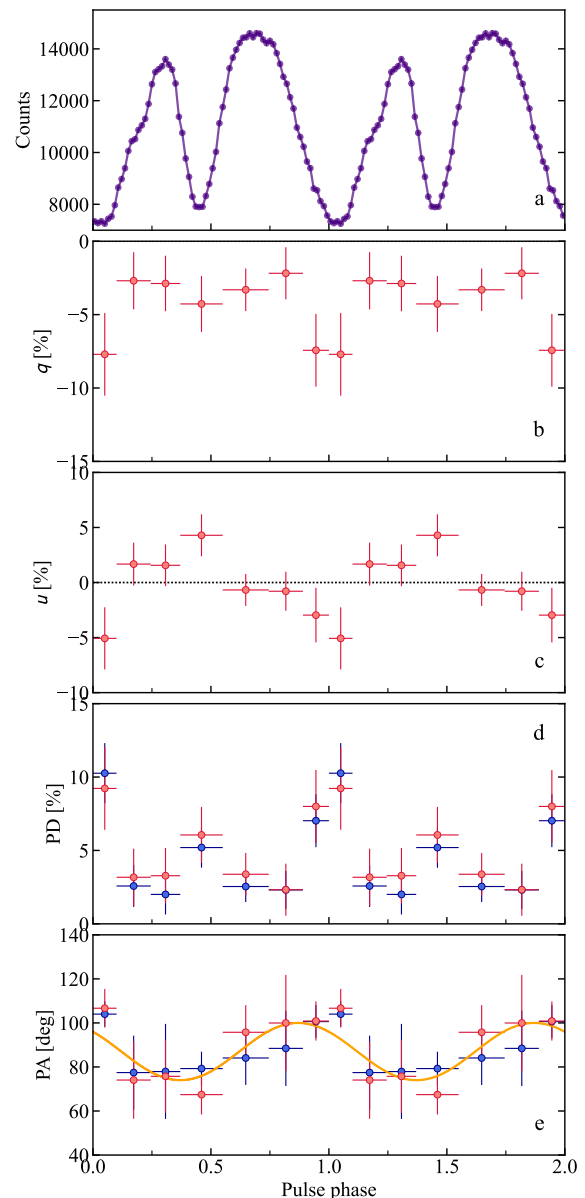


Fig. 7. Results from the pulse-phase-resolved analysis of SMC X-1 in the 2–8 keV range combining data from all DUs and using non-uniform phase-binning. Panel (a): Pulse profile. Panels (b) and (c): Dependence of the Stokes q and u parameters obtained from the `pcube` algorithm on the pulse phase. Panels (d) and (e): PD and PA obtained with `pcube` and from the phase-resolved spectro-polarimetric analysis using `xSPEC` (shown by the red and blue symbols, respectively). The orange curve in panel (e) shows the best-fit RVM to the combined data set.

ized Stokes q and u parameters in the individual observations, as displayed in Fig. 6. Similarly, we used the same steps to perform a phase-resolved polarimetric analysis of the combined data set, which indicated an anti-correlation between the PD and flux. Therefore, we applied a non-uniform phase-binning to the combined data set, with the phase bins chosen to cover the maxima and minima of the pulse profile. The results in the 2–8 keV energy range are given in Table 4 and are shown in Fig. 7.

To fully account for the spectral shape and the energy dispersion, we performed a spectro-polarimetric analysis according to the following steps. Source Stokes I , Q , and U spectra were extracted using the `xpbin` tool’s `PHA1`, `PHA1Q`, and `PHA1U` algorithms, which produce a full data set made up of nine spectra,

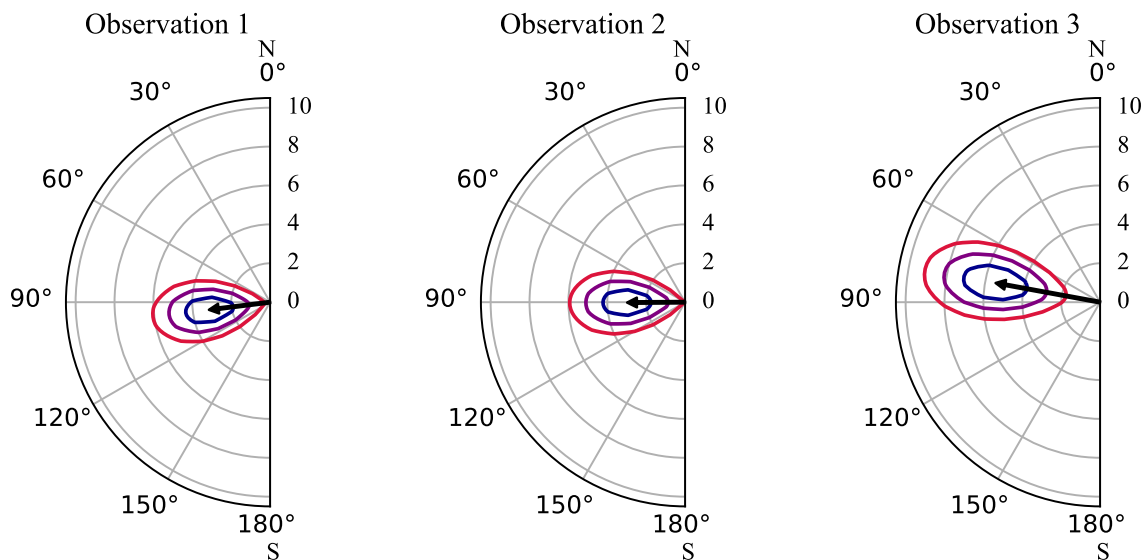


Fig. 8. Polarization vectors of SMC X-1 from the results of the phase-averaged spectro-polarimetric analysis of Obs. 1 (*left*), Obs. 2 (*center*), and Obs. 3 (*right*). Contours at 68.3%, 95.45%, and 99.73% confidence levels calculated for two degrees of freedom are shown in blue, purple, and red, respectively.

Table 4. Normalized q and u Stokes parameters and PD and PA in different phase bins obtained from the pcube algorithm (combined data set; dip excluded).

Phase	q (%)	u (%)	PD (%)	PA (deg)
0.000–0.100	-7.7 ± 2.8	-5.1 ± 2.8	9.2 ± 2.8	107 ± 9
0.100–0.245	-2.7 ± 1.9	1.7 ± 1.9	3.2 ± 1.9	74 ± 18
0.245–0.370	-2.9 ± 1.9	1.6 ± 1.9	3.3 ± 1.9	76 ± 17
0.370–0.550	-4.3 ± 1.9	4.3 ± 1.9	6.1 ± 1.9	67 ± 9
0.550–0.745	-3.3 ± 1.5	-0.7 ± 1.5	3.4 ± 1.5	96 ± 12
0.745–0.890	-2.2 ± 1.8	-0.8 ± 1.8	2.3 ± 1.8	100 ± 22
0.890–1.000	-7.4 ± 2.5	-3.0 ± 2.5	8.0 ± 2.5	101 ± 9

Notes. The uncertainties are given at the 68.3% (1σ) confidence level.

three for each DU. We fitted all nine spectra simultaneously with XSPEC.

The spectral continuum of SMC X-1 has been described by a number of different phenomenological models, however, it is usually represented by an absorbed power law with a high-energy cut-off and a soft component, as well as a weak iron line at about 6.4 keV. Taking into consideration the energy range and resolution of IXPE, we adopted a simplified model consisting of an absorbed powerlaw, the polconst polarization model (energy-independent PA and PD), as well as a cross-calibration constant accounting for possible discrepancies between the different DUs, where the value for DU1 was fixed at unity. The final spectral model,

$$\text{tbabs} \times \text{polconst} \times \text{powerlaw} \times \text{const},$$

was applied to both the phase-averaged and phase-resolved data. The spectral analysis was performed over the full 2–8 keV energy range of IXPE. The steppar command in XSPEC was used to create the confidence contours for the phase-averaged polarization measurements of Obs. 1, 2 and 3, and the resulting contour plots at 68.3%, 95.45%, and 99.73% confidence levels are shown in Fig. 8. Table 5 lists the spectral parameters for the best-fit models from the results of the phase-averaged spectro-

polarimetric analysis for Obs. 1, 2, and 3. We find significant detection of polarization corresponding to 3.3σ , 3.0σ , and 4.7σ for Obs. 1, 2, and 3, respectively, determined for two degrees of freedom.

To examine the possibility of any energy-dependence of the polarization properties during the individual observations, the polconst polarization model was replaced with the pollin model (linear energy dependence of the PD and PA) and the polpow model (power law energy dependence of the PD and PA). Neither model resulted in a significant improvement of the fit.

Considering the similar values of the spectral parameters between all three observations, a joint spectro-polarimetric fit was performed at the next step by fitting the spectra of all three observations simultaneously (with a total of 27 spectra, nine per observation). The power-law normalization was allowed to vary between the observations. The results of the phase-averaged spectro-polarimetric analysis of the combined set of spectra can be found in Table 5. Similarly to the analysis of the separate observations, the energy-dependence of the polarization properties for the joint fit was tested by replacing the polconst polarization model with the pollin model and polpow model. However, neither model significantly improved the fit.

Next, a phase-resolved spectro-polarimetric analysis was performed by separating the data into seven non-uniform phase-bins. This was achieved by extracting Stokes I , Q , and U spectra individually for each phase bin, using the PHA1, PHA1Q, and PHA1U algorithms of the xpbins tool.

The phase-resolved I , Q , and U spectra were fitted with the same model as used for the phase-averaged analysis, and the cross-calibration constants for DU2 and DU3 were set to the values of the phase-averaged analysis (see Table 5). The steppar command in XSPEC was used to create the confidence contours for the phase-resolved polarization measurements, and the resulting contour plots at 68.3%, 95.45%, and 99.73% confidence levels are shown in Fig. 9. The results of the phase-resolved spectro-polarimetric analysis of the combined data set are summarized in Table 6. We find significant detection of polarization in three out of seven phase bins, and marginal detections in the remaining bins.

Table 5. Spectral parameters for the best-fit model obtained from the phase-averaged spectro-polarimetric analysis with `xspec` for observations 1, 2, and 3.

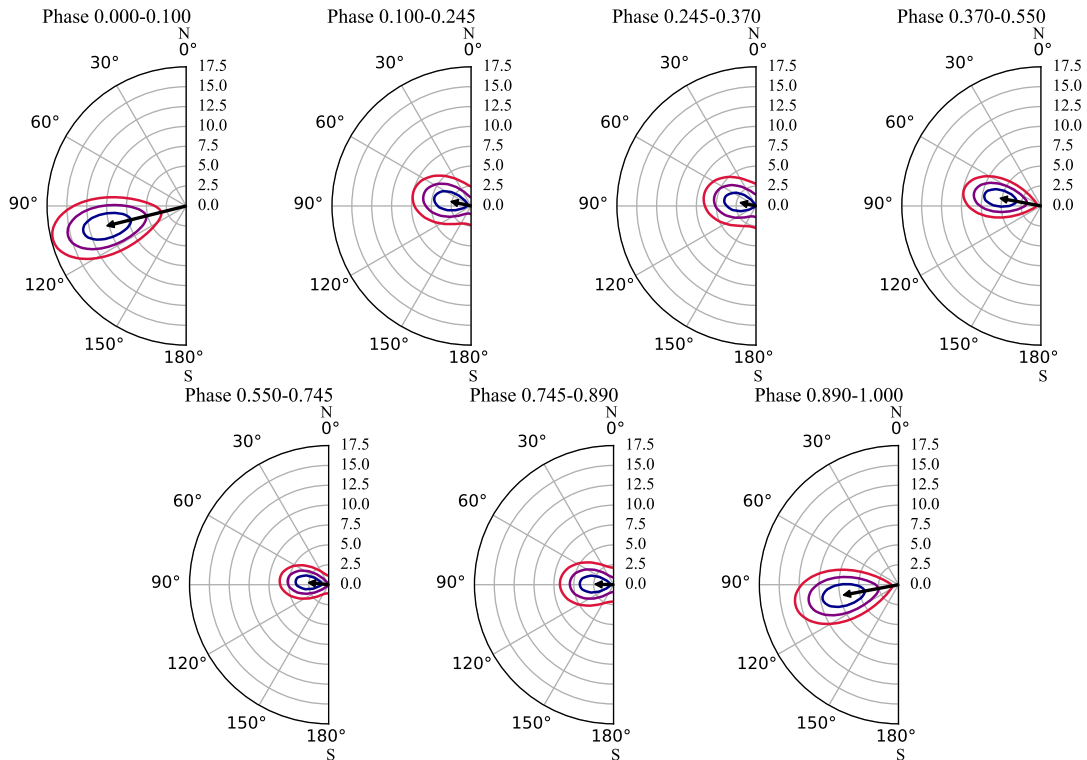
Component	Parameter	Unit	Obs. 1	Obs. 2	Obs. 3	Obs. 1–3
tbabs	N_{H}	10^{22} cm^{-2}	0.23 ± 0.07	0.31 ± 0.07	0.43 ± 0.09	0.31 ± 0.05
powerlaw	Photon index		1.00 ± 0.02	1.02 ± 0.02	1.02 ± 0.02	1.01 ± 0.01
polconst	PD	%	3.2 ± 0.8	3.0 ± 0.9	5.5 ± 1.1	3.5 ± 0.5
	PA	deg	97 ± 8	90 ± 8	80 ± 6	89 ± 4
constant	const _{DU2}		1.019 ± 0.005	1.021 ± 0.005	1.026 ± 0.006	1.021 ± 0.003
	const _{DU3}		1.002 ± 0.005	1.000 ± 0.005	1.023 ± 0.006	1.001 ± 0.003
	Flux _{2–8 keV}	$10^{-10} \text{ erg s}^{-1} \text{ cm}^{-2}$	5.10 ± 0.07	4.92 ± 0.07	4.65 ± 0.07	–
	$L_{2–8 \text{ keV}}^{(a)}$	$10^{38} \text{ erg s}^{-1}$	2.3	2.2	2.1	–
	χ^2 (d.o.f.)		1332.1 (1259)	1240.0 (1262)	1256.9 (1214)	3845.3 (3747)

Notes. The uncertainties are given at the 68.3% (1σ) confidence level and were obtained using the `error` command in `xspec` with $\Delta\chi^2 = 1$ for one parameter of interest. ^(a) Luminosity is computed using the distance of $d = 61$ kpc (Hilditch et al. 2005).

Table 6. Spectro-polarimetric parameters in different pulse-phase bins for the combined data set obtained with `xspec`.

Phase	N_{H} (10^{22} cm^{-2})	Photon index	PD (%)	PA (deg)	$\chi^2/\text{d.o.f.}$
0.000–0.100	0.31	1.05 ± 0.02	10.3 ± 2.0	104 ± 6	2038/2058
0.100–0.245	0.25 ± 0.13	0.96 ± 0.03	2.6 ± 1.4	78 ± 17	2679/2621
0.245–0.370	0.83 ± 0.12	1.10 ± 0.03	2.0 ± 1.4	78 ± 22	2699/2657
0.370–0.550	0.31	1.11 ± 0.01	5.2 ± 1.4	79 ± 8	2623/2658
0.550–0.745	0.56 ± 0.09	1.06 ± 0.02	2.5 ± 1.1	84 ± 12	3032/3047
0.745–0.890	0.38 ± 0.11	1.04 ± 0.03	2.3 ± 1.3	88 ± 17	2743/2759
0.890–1.000	0.31	1.08 ± 0.01	7.0 ± 1.8	101 ± 8	2230/2247

Notes. For the first, fourth, and last phase bin, the value of N_{H} was fixed to the value of the phase-averaged spectro-polarimetric analysis for the combined data set. The uncertainties computed using the `error` command are given at the 68.3% (1σ) confidence level ($\Delta\chi^2 = 1$ for one parameter of interest).


Fig. 9. Polarization vectors of SMC X-1 from the results of the phase-resolved spectro-polarimetric analysis of the combined data set. Contours at 68.3%, 95.45%, and 99.73% confidence levels calculated for two degrees of freedom are shown in blue, purple, and red, respectively.

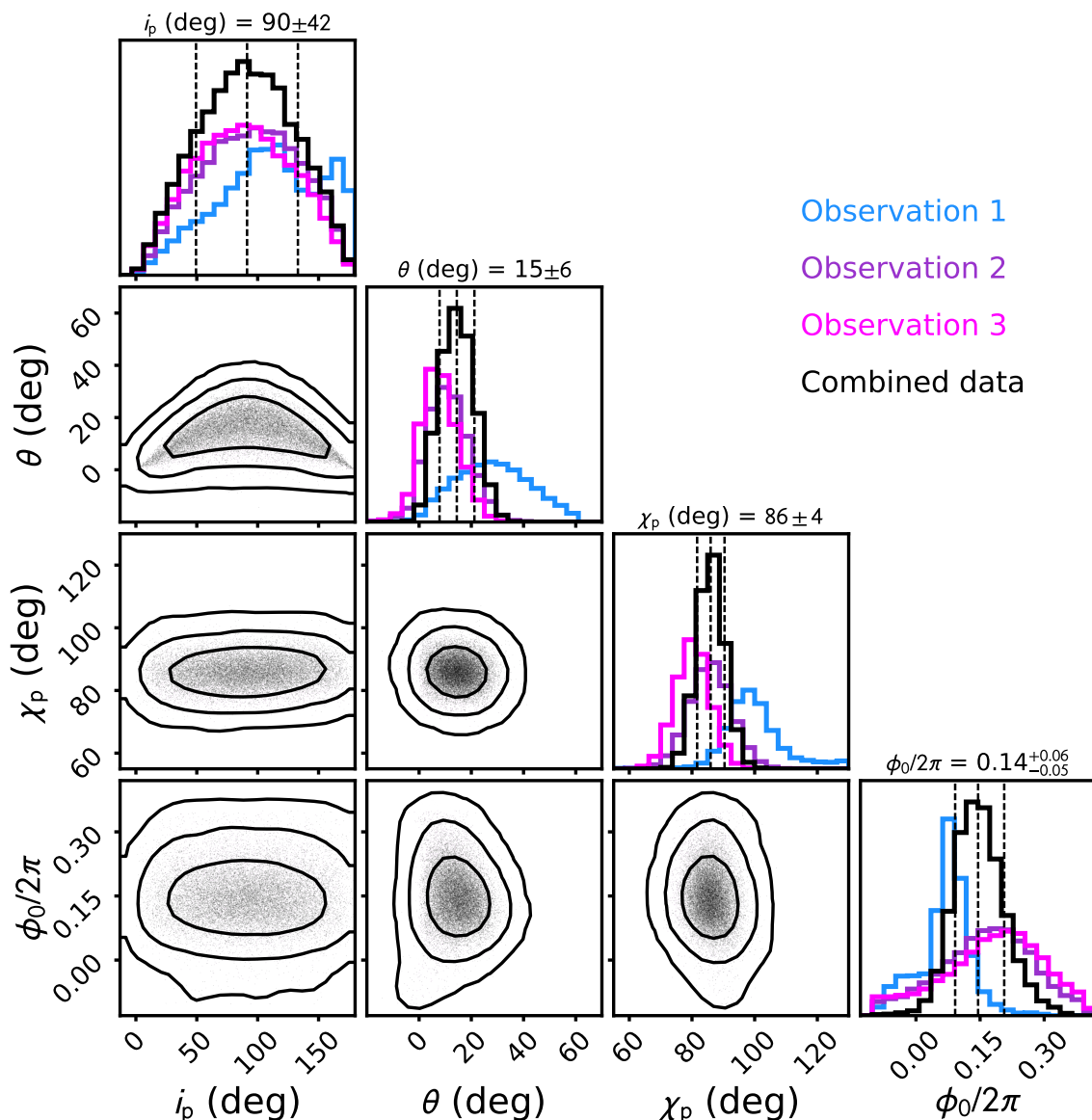


Fig. 10. Corner plot of the posterior distribution for parameters of the RVM model fitted directly to the (q, u) values using the likelihood function given by Eq. (2). The two-dimensional contours correspond to 68.3%, 95.45% and 99.73% confidence levels and are shown for the combined data set. The histograms show the normalized one-dimensional distributions for a given parameter derived from the posterior samples and are displayed for the individual observations and the combined data set.

Table 7. Best-fit RVM parameters for the separate observations of SMC X-1, as well as the combined data set.

Parameter	Obs. 1	Obs. 2	Obs. 3	Obs. 1–3
i_p (deg)	98^{+38}_{-41}	100^{+40}_{-45}	88^{+43}_{-43}	91^{+41}_{-42}
θ (deg)	23^{+14}_{-14}	14^{+8}_{-8}	6^{+7}_{-6}	13^{+7}_{-6}
χ_p (deg)	98^{+13}_{-6}	86^{+8}_{-7}	80^{+6}_{-5}	87^{+4}_{-4}
$\phi_0/2\pi$	$0.07^{+0.05}_{-0.04}$	$0.14^{+0.08}_{-0.09}$	$0.18^{+0.17}_{-0.15}$	$0.12^{+0.08}_{-0.06}$

4. Discussion

4.1. Determination of pulsar geometry

The rotating vector model (RVM; Radhakrishnan & Cooke 1969; Meszaros et al. 1988) can be used to constrain the pulsar geometry. The geometrical properties of several XRP observed by IXPE have already been obtained (Doroshenko et al. 2022;

Tsygankov et al. 2022; Mushtukov et al. 2023; Marshall et al. 2022; Tsygankov et al. 2023; Malacaria et al. 2023; Doroshenko et al. 2023; Suleimanov et al. 2023; Heyl et al. 2024; Zhao et al. 2024). If the radiation is assumed to be dominated by ordinary mode (O-mode) photons, the PA is given by equation (30) from Poutanen (2020):

$$\tan(\text{PA} - \chi_p) = \frac{-\sin \theta \sin(\phi - \phi_0)}{\sin i_p \cos \theta - \cos i_p \sin \theta \cos(\phi - \phi_0)}, \quad (1)$$

where χ_p is the position angle (measured from north to east) of the pulsar angular momentum, i_p is the inclination of the pulsar spin to the line of sight, θ comprises the angle between the magnetic dipole and the spin axis, and ϕ_0 equals the phase when the northern magnetic pole passes in front of the observer.

If the radiation escapes predominantly in the extraordinary mode (X-mode), the position angle of the pulsar angular momentum is $\chi_p \pm 90^\circ$. The PA does not depend on the PD of the radiation escaping from the surface of the NS in the no-relativistic

RVM. The polarization plane actually rotates as the radiation travels through the NS magnetosphere, up to the adiabatic radius. At such a distance, the dipole magnetic field component will dominate, and under these conditions, the RVM is applicable. Only when the NS is rotating rapidly will general relativistic effects have an effect on the polarization plane (Poutanen 2020).

We can fit the RVM to the measured Stokes q and u parameters, which are normally distributed, as a function of the pulsar phase. Because the PA is not normally distributed, we use the probability density function of the PA, ψ , from Naghizadeh-Khouei & Clarke (1993):

$$G(\psi) = \frac{1}{\sqrt{\pi}} \left\{ \frac{1}{\sqrt{\pi}} + \eta e^{\eta^2} [1 + \operatorname{erf}(\eta)] \right\} e^{-p_0^2/2}. \quad (2)$$

Here, $p_0 = \sqrt{q^2 + u^2}/\sigma_p$ is the measured PD in units of the error, $\eta = p_0 \cos[2(\psi - \psi_0)]/\sqrt{2}$, $\psi_0 = \frac{1}{2} \arctan(u/q)$ is the central PA obtained from the Stokes parameters, and erf is the error function.

The RVM can be fitted to the pulse-phase dependent (q , u) obtained from `pcube` using the affine invariant Markov Chain Monte Carlo (MCMC) ensemble sampler `emcee` package of `PYTHON` (Foreman-Mackey et al. 2013) and applying the likelihood function $L = \prod_i G(\psi_i)$ with the product taken over all phase bins. The RVM was fitted to both the separate observations and the combined set of observations. The best-fit RVM parameters are given in Table 7. The covariance plot for the parameters is shown in Fig. 10. The RVM provides an overall good fit to the combined data set and the separate observations.

We see in Fig. 10 that the position angle of the pulsar χ_p shows changes over the course of the observations, decreasing in roughly 10° decrements. Similarly, the PD also exhibits changes between the individual observations, increasing over time and with decreasing luminosities. The observations of SMC X-1 were carried out during the high-state, corresponding to different super-orbital phases. The super-orbital variability is generally associated with the precession of the accretion disk, causing periodical obscuration of the central source. Scattering in the wind of the disk may introduce a polarized component which could lead to variations in the PA pulse phase dependence depending on the super-orbital phase. Similar conclusions have been drawn for other XRP observed with IXPE that also display variations in the pulse phase dependence of the PA (Doroshenko et al. 2023; Zhao et al. 2024; Poutanen et al. 2024).

4.2. Anti-correlation of luminosity and PD

SMC X-1 is the brightest XRP observed by IXPE so far. The super-critical luminosity indicates the presence of an accretion column (Basko & Sunyaev 1976), which is expected to result in high PDs (Caiazzo & Heyl 2021). However, the PD for SMC X-1 is relatively low, consistent with other XRPs observed by IXPE.

The lower degree of linear polarization at higher apparent luminosities in SMC X-1 can be related to the geometry of the emitting region in the super-critical regime of accretion and/or the contribution of the magnetospheric accretion flow. The appearance of an accretion column at luminosities $\gtrsim 10^{37} \text{ erg s}^{-1}$ results in the illumination of the NS surface, and the contribution of reflected X-rays (see, e.g., Poutanen et al. 2013; Postnov et al. 2015) to the apparent photon energy flux and the polarization. In this case, the PD can be reduced due to the possibility of different contributions of X- and O-modes to the total energy flux.

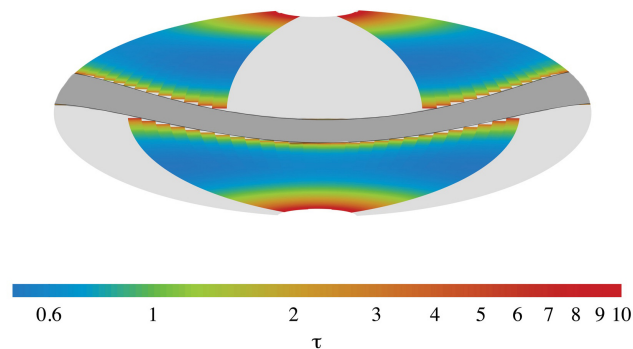


Fig. 11. Map of the optical thickness τ (due to the Compton scattering) distribution over the magnetosphere of SMC X-1 calculated using the model of Mushtukov et al. (2024) as viewed from the NS center in Aitoff projection with the z -axis aligned along the magnetic dipole. The color represents the distribution of the optical thickness. The gray belt is the region where the accretion disk touches NS magnetosphere and where τ is infinite. The magnetosphere is covered only partially because of the assumed 15° inclination of magnetic dipole with respect to the disk axis. The flow is transparent at azimuthal angle around 0° in the northern hemisphere and at the angle 180° in the southern hemisphere, because there is no accretion along these field lines. The NS spin axis is assumed to be aligned with the disk rotation axis. We used the following parameters: $L = 2 \times 10^{38} \text{ erg s}^{-1}$ and $R_m = 5 \times 10^7 \text{ cm}$.

At luminosities $\gtrsim 10^{38} \text{ erg s}^{-1}$, the accretion flow between the inner disk radius and the NS surface can be optically thick for Compton scattering, and therefore scatters a fraction of X-ray photons (Mushtukov et al. 2017, 2019; Brice et al. 2023). Figure 11 illustrates the expected distribution of the optical thickness over the magnetospheric surface of the NS in SMC X-1 calculated following the model of Mushtukov et al. (2024). The major process responsible for the opacity of the magnetospheric accretion flow at $E > 1 \text{ keV}$ is Compton scattering. Because of the magnetic dipole inclination with respect to the rotational axis of the NS, the accretion flow covers only a fraction of the magnetospheric surface. The optical thickness is expected to be larger (up to $\tau \sim 10$) in regions located close to the plane of the accretion disk and close to the NS surface, because of the relatively high local surface density of the flow. The minimal optical thickness in the regions of the magnetosphere covered by the accretion flow is $\tau_{\min} \approx 0.7$.

For the observed luminosity in SMC X-1 ($\sim 2 \times 10^{38} \text{ erg s}^{-1}$) and a NS rotation axis aligned with the disk axis, the magnetospheric flow scatters up to 40% of X-ray photons depending on the beam pattern of X-ray emission of the NS surface. For an inclined rotator, the contribution of photons scattered in the magnetosphere to the total flux depends on the observer's viewing angle, but remains close to 40% on average. Because the magnetospheric radius R_m is expected to be larger than the adiabatic radius R_{ad} (González Caniulef et al. 2016; Taverna & Turolla 2024)

$$R_m > R_{\text{ad}} \approx 1.2 \times 10^7 \left(\frac{B}{10^{12} \text{ G}} \right)^{2/5} \left(\frac{E}{1 \text{ keV}} \right)^{1/5} \left(\frac{R_{\text{NS}}}{10^6 \text{ cm}} \right)^{6/5} \text{ cm}, \quad (3)$$

the scattering of X-ray photons at the magnetospheric surface can result in depolarization. The higher the luminosity and optical thickness of the flow, the lower the PD.

The appearance of an optically thick flow that covers only a fraction of the NS magnetosphere in SMC X-1 is aligned with the presence of a pulsating soft blackbody component at energies

< 2 keV reported in this object (see, e.g., Paul et al. 2002). Note, however, that the soft excess in SMC X-1 can also be explained by the reflection of X-ray photons off the accretion disk twisted close to the inner radius (see Hickox & Vrtilek 2005). If this is indeed the case, both the PD and the PA can be affected by X-ray reflection from such a disk.

5. Summary

SMC X-1 was observed by IXPE three separate times around 2023 December 10–20, during the high-state of the super-orbital period at luminosities of $L \sim 2 \times 10^{38}$ erg s⁻¹. The results of the polarimetric analysis of SMC X-1 can be summarized as follows:

1. A significant polarization was detected during all three observations (spectro-polarimetric analysis), with values of the phase-averaged PD and PA corresponding to $3.2 \pm 0.8\%$ and $97^\circ \pm 8^\circ$ for Observation 1, $3.0 \pm 0.9\%$ and $90^\circ \pm 8^\circ$ for Observation 2, and $5.5 \pm 1.1\%$ and $80^\circ \pm 6^\circ$ for Observation 3. There is an indication of a trend in the behavior of the PD and PA over time.
2. There is no evidence for any energy-dependent nature of the polarization properties found in the polarimetric analysis using pcube algorithm or in the spectro-polarimetric analysis. This holds for the phase-averaged analysis, as well as for the phase-resolved analysis.
3. The phase-resolved spectro-polarimetric analysis found significant detection of polarization in three out of seven phase bins, with the PD ranging between $\sim 2\%$ and $\sim 10\%$, and a corresponding range in the PA of $\sim 70^\circ$ to $\sim 100^\circ$. The PD displays an anti-correlation with the flux amplitude.
4. The phase-resolved polarimetric analysis of the individual observations suggests a difference in the behavior of the normalized Stokes q and u that indicate a change in polarization properties over time. Using the RVM to model the PA pulse phase dependence, we determine the pulsar geometry for the separate observations. The position angle of the pulsar rotation axis displays an evolution with super-orbital phase supporting the idea of a NS and/or accretion disk precession in this source.

Acknowledgements. The Imaging X-ray Polarimetry Explorer (IXPE) is a joint US and Italian mission. The US contribution is supported by the National Aeronautics and Space Administration (NASA) and led and managed by its Marshall Space Flight Center (MSFC), with industry partner Ball Aerospace (contract NNM15AA18C). The Italian contribution is supported by the Italian Space Agency (Agenzia Spaziale Italiana, ASI) through contract ASI-OHBI-2022-13-I.0, agreements ASI-INAF-2022-19-HH.0 and ASI-INFN-2017.13-HO, and its Space Science Data Center (SSDC) with agreements ASI-INAF-2022-14-HH.0 and ASI-INFN 2021-43-HH.0, and by the Istituto Nazionale di Astrofisica (INAF) and the Istituto Nazionale di Fisica Nucleare (INFN) in Italy. This research used data products provided by the IXPE Team (MSFC, SSCD, INAF, and INFN) and distributed with additional software tools by the High-Energy Astrophysics Science Archive Research Center (HEASARC), at NASA Goddard Space Flight Center (GSFC). This research has been supported by the Academy of Finland grants 333112 and 349144 (SVF, SST, JP, VL), the German Academic Exchange Service (DAAD) travel grant 57525212 (VD, VFS), UKRI Stephen Hawking fellowship (AAM), and Deutsche Forschungsgemeinschaft (DFG) grant WE 1312/59-1 (VFS). SVF acknowledges the support of the Vilho, Yrjö, and Kalle Väisälä foundation. The work of RT, GM, FM and PS was partially funded by the Italian Ministry of University and Research (MUR) through grant PRIN 2022LWPEXW. IL was supported by the NASA Postdoctoral Program at the Marshall Space Flight Center, administered by Oak Ridge Associated Universities under contract with NASA.

References

Angelini, L., Stella, L., & White, N. E. 1991, *ApJ*, 371, 332

- Arnaud, K. A. 1996, in ASP Conf. Ser., Vol. 101, *Astronomical Data Analysis Software and Systems V*, ed. G. H. Jacoby & J. Barnes (San Francisco: Astron. Soc. Pac.), 17
- Baldini, L., Barbanera, M., Bellazzini, R., et al. 2021, *Astroparticle Physics*, 133, 102628
- Basko, M. M., & Sunyaev, R. A. 1976, *MNRAS*, 175, 395
- Bonnet-Bidaud, J. M., & van der Klis, M. 1981, *A&A*, 97, 134
- Brice, N., Zane, S., Taverna, R., Turolla, R., & Wu, K. 2023, *MNRAS*, 525, 4176
- Caiazzo, I., & Heyl, J. 2021, *MNRAS*, 501, 109
- Clarkson, W. I., Charles, P. A., Coe, M. J., et al. 2003, *MNRAS*, 339, 447
- Dage, K. C., Clarkson, W. I., Charles, P. A., Laycock, S. G. T., & Shih, I. C. 2019, *MNRAS*, 482, 337
- Di Marco, A., Costa, E., Muleri, F., et al. 2022, *AJ*, 163, 170
- Di Marco, A., Soffitta, P., Costa, E., et al. 2023, *AJ*, 165, 143
- Doroshenko, V., Poutanen, J., Tsygankov, S. S., et al. 2022, *Nature Astronomy*, 6, 1433
- Doroshenko, V., Poutanen, J., Heyl, J., et al. 2023, *A&A*, 677, A57
- Foreman-Mackey, D., Hogg, D. W., Lang, D., & Goodman, J. 2013, *PASP*, 125, 306
- Forsblom, S. V., Poutanen, J., Tsygankov, S. S., et al. 2023, *ApJ*, 947, L20
- Gehrels, N., Chincarini, G., Giommi, P., et al. 2004, *ApJ*, 611, 1005
- González Caniulef, D., Zane, S., Taverna, R., Turolla, R., & Wu, K. 2016, *MNRAS*, 459, 3585
- Heyl, J., Doroshenko, V., González-Caniulef, D., et al. 2024, *Nature Astronomy*, in press, arXiv:2311.03667
- Hickox, R. C., & Vrtilek, S. D. 2005, *ApJ*, 633, 1064
- Hilditch, R. W., Howarth, I. D., & Harries, T. J. 2005, *MNRAS*, 357, 304
- Hu, C.-P., Chou, Y., Yang, T.-C., & Su, Y.-H. 2013, *ApJ*, 773, 58
- Hu, C.-P., Mihara, T., Sugizaki, M., Ueda, Y., & Enoto, T. 2019, *ApJ*, 885, 123
- Kaaret, P., Feng, H., & Roberts, T. P. 2017, *ARA&A*, 55, 303
- Kislat, F., Clark, B., Beilicke, M., & Krawczynski, H. 2015, *Astroparticle Physics*, 68, 45
- Leong, C., Kellogg, E., Gursky, H., Tananbaum, H., & Giacconi, R. 1971, *ApJ*, 170, L67
- Lucke, R., Yentis, D., Friedman, H., Fritz, G., & Shulman, S. 1976, *ApJ*, 206, L25
- Malacaria, C., Heyl, J., Doroshenko, V., et al. 2023, *A&A*, 675, A29
- Marshall, H. L., Ng, M., Rogantini, D., et al. 2022, *ApJ*, 940, 70
- Meszáros, P., Novick, R., Szentgyorgyi, A., Chanan, G. A., & Weisskopf, M. C. 1988, *ApJ*, 324, 1056
- Moon, D.-S., Eikenberry, S. S., & Wasserman, I. M. 2003, *ApJ*, 582, L91
- Mushtukov, A., & Tsygankov, S. 2024, in *Handbook of X-ray and Gamma-ray Astrophysics*, ed. C. Bambi & A. Santangelo (Singapore: Springer), 4105
- Mushtukov, A. A., Ingram, A., Middleton, M., Nagirner, D. I., & van der Klis, M. 2019, *MNRAS*, 484, 687
- Mushtukov, A. A., Ingram, A., Suleimanov, V. F., et al. 2024, *MNRAS*, 530, 730
- Mushtukov, A. A., Suleimanov, V. F., Tsygankov, S. S., & Ingram, A. 2017, *MNRAS*, 467, 1202
- Mushtukov, A. A., Tsygankov, S. S., Poutanen, J., et al. 2023, *MNRAS*, 524, 2004
- Naghizadeh-Khouei, J., & Clarke, D. 1993, *A&A*, 274, 968
- Paul, B., Nagase, F., Endo, T., et al. 2002, *ApJ*, 579, 411
- Postnov, K. A., Gornostaev, M. I., Klochkov, D., et al. 2015, *MNRAS*, 452, 1601
- Poutanen, J. 2020, *A&A*, 641, A166
- Poutanen, J., Mushtukov, A. A., Suleimanov, V. F., et al. 2013, *ApJ*, 777, 115
- Poutanen, J., Tsygankov, S. S., Doroshenko, V., et al. 2024, *A&A*, submitted, arXiv:2405.08107
- Price, R. E., Groves, D. J., Rodrigues, R. M., et al. 1971, *ApJ*, 168, L7
- Radhakrishnan, V., & Cooke, D. J. 1969, *Astrophys. Lett.*, 3, 225
- Rai, B., Pradhan, P., & Paul, B. C. 2018, *Research in Astronomy and Astrophysics*, 18, 148
- Raichur, H., & Paul, B. 2010, *MNRAS*, 401, 1532
- Reig, P. 2011, *Ap&SS*, 332, 1
- Schreier, E., Giacconi, R., Gursky, H., Kellogg, E., & Tananbaum, H. 1972, *ApJ*, 178, L71
- Soffitta, P., Baldini, L., Bellazzini, R., et al. 2021, *AJ*, 162, 208
- Suleimanov, V. F., Forsblom, S. V., Tsygankov, S. S., et al. 2023, *A&A*, 678, A119
- Taverna, R., & Turolla, R. 2024, *Galaxies*, 12, 6
- Trowbridge, S., Nowak, M. A., & Wilms, J. 2007, *ApJ*, 670, 624
- Tsygankov, S. S., Doroshenko, V., Poutanen, J., et al. 2022, *ApJ*, 941, L14
- Tsygankov, S. S., Doroshenko, V., Mushtukov, A. A., et al. 2023, *A&A*, 675, A48
- van der Meer, A., Kaper, L., van Kerkwijk, M. H., Heemskerck, M. H. M., & van den Heuvel, E. P. J. 2007, *A&A*, 473, 523
- Weisskopf, M. C., Soffitta, P., Baldini, L., et al. 2022, *JATIS*, 8, 026002
- Wojdowski, P., Clark, G. W., Levine, A. M., Woo, J. W., & Zhang, S. N. 1998, *ApJ*, 502, 253
- Zhao, Q. C., Li, H. C., Tao, L., et al. 2024, *MNRAS*, arXiv:2405.00509 [astro-ph.HE]

-
- ¹ Department of Physics and Astronomy, FI-20014 University of Turku, Finland
e-mail: sofia.v.forsblom@utu.fi
- ² Institut für Astronomie und Astrophysik, Universität Tübingen, Sand 1, D-72076 Tübingen, Germany
- ³ Astrophysics, Department of Physics, University of Oxford, Denys Wilkinson Building, Keble Road, Oxford OX1 3RH, UK
- ⁴ MIT Kavli Institute for Astrophysics and Space Research, Massachusetts Institute of Technology, 77 Massachusetts Avenue, Cambridge, MA 02139, USA
- ⁵ INAF Istituto di Astrofisica e Planetologia Spaziali, Via del Fosso del Cavaliere 100, 00133 Roma, Italy
- ⁶ Dipartimento di Fisica, Università degli Studi di Roma “Tor Vergata”, Via della Ricerca Scientifica 1, 00133 Roma, Italy
- ⁷ Dipartimento di Fisica, Università degli Studi di Roma “La Sapienza”, Piazzale Aldo Moro 5, 00185 Roma, Italy
- ⁸ International Space Science Institute, Hallerstrasse 6, 3012 Bern, Switzerland
- ⁹ Dipartimento di Fisica, Università degli Studi di Milano, Via Celoria 16, I-20133 Milano, Italy
- ¹⁰ INAF Osservatorio Astronomico di Cagliari, Via della Scienza 5, 09047 Selargius (CA), Italy
- ¹¹ Dipartimento di Fisica e Astronomia, Università degli Studi di Padova, Via Marzolo 8, 35131 Padova, Italy
- ¹² Instituto de Astrofísica de Andalucía – CSIC, Glorieta de la Astronomía s/n, 18008 Granada, Spain
- ¹³ INAF Osservatorio Astronomico di Roma, Via Frascati 33, 00040 Monte Porzio Catone (RM), Italy
- ¹⁴ Space Science Data Center, Agenzia Spaziale Italiana, Via del Politecnico snc, 00133 Roma, Italy
- ¹⁵ Istituto Nazionale di Fisica Nucleare, Sezione di Pisa, Largo B. Pontecorvo 3, 56127 Pisa, Italy
- ¹⁶ Dipartimento di Fisica, Università di Pisa, Largo B. Pontecorvo 3, 56127 Pisa, Italy
- ¹⁷ NASA Marshall Space Flight Center, Huntsville, AL 35812, USA
- ¹⁸ Dipartimento di Matematica e Fisica, Università degli Studi Roma Tre, via della Vasca Navale 84, 00146 Roma, Italy
- ¹⁹ Istituto Nazionale di Fisica Nucleare, Sezione di Torino, Via Pietro Giuria 1, 10125 Torino, Italy
- ²⁰ Dipartimento di Fisica, Università degli Studi di Torino, Via Pietro Giuria 1, 10125 Torino, Italy
- ²¹ INAF Osservatorio Astrofisico di Arcetri, Largo Enrico Fermi 5, 50125 Firenze, Italy
- ²² Dipartimento di Fisica e Astronomia, Università degli Studi di Firenze, Via Sansone 1, 50019 Sesto Fiorentino (FI), Italy
- ²³ Istituto Nazionale di Fisica Nucleare, Sezione di Firenze, Via Sansone 1, 50019 Sesto Fiorentino (FI), Italy
- ²⁴ Agenzia Spaziale Italiana, Via del Politecnico snc, 00133 Roma, Italy
- ²⁵ Science and Technology Institute, Universities Space Research Association, Huntsville, AL 35805, USA
- ²⁶ Istituto Nazionale di Fisica Nucleare, Sezione di Roma “Tor Vergata”, Via della Ricerca Scientifica 1, 00133 Roma, Italy
- ²⁷ Department of Physics and Kavli Institute for Particle Astrophysics and Cosmology, Stanford University, Stanford, California 94305, USA
- ²⁸ Astronomical Institute of the Czech Academy of Sciences, Boční II 1401/1, 14100 Praha 4, Czech Republic
- ²⁹ RIKEN Cluster for Pioneering Research, 2-1 Hirosawa, Wako, Saitama 351-0198, Japan
- ³⁰ X-ray Astrophysics Laboratory, NASA Goddard Space Flight Center, Greenbelt, MD 20771, USA
- ³¹ Yamagata University, 1-4-12 Kojirakawa-machi, Yamagata-shi 990-8560, Japan
- ³² Osaka University, 1-1 Yamadaoka, Suita, Osaka 565-0871, Japan
- ³³ University of British Columbia, Vancouver, BC V6T 1Z4, Canada
- ³⁴ International Center for Hadron Astrophysics, Chiba University, Chiba 263-8522, Japan
- ³⁵ Institute for Astrophysical Research, Boston University, 725 Commonwealth Avenue, Boston, MA 02215, USA
- ³⁶ Department of Astrophysics, St. Petersburg State University, Universitetskyy pr. 28, Petrodvoretz, 198504 St. Petersburg, Russia
- ³⁷ Department of Physics and Astronomy and Space Science Center, University of New Hampshire, Durham, NH 03824, USA
- ³⁸ Physics Department and McDonnell Center for the Space Sciences, Washington University in St. Louis, St. Louis, MO 63130, USA
- ³⁹ Institute of Astrophysics, Foundation for Research and Technology-Hellas, GR-70013 Heraklion, Greece
- ⁴⁰ Istituto Nazionale di Fisica Nucleare, Sezione di Napoli, Strada Comunale Cinthia, 80126 Napoli, Italy
- ⁴¹ Université de Strasbourg, CNRS, Observatoire Astronomique de Strasbourg, UMR 7550, 67000 Strasbourg, France
- ⁴² Graduate School of Science, Division of Particle and Astrophysical Science, Nagoya University, Furo-cho, Chikusa-ku, Nagoya, Aichi 464-8602, Japan
- ⁴³ Hiroshima Astrophysical Science Center, Hiroshima University, 1-3-1 Kagamiyama, Higashi-Hiroshima, Hiroshima 739-8526, Japan
- ⁴⁴ Department of Physics and Astronomy, Louisiana State University, Baton Rouge, LA 70803, USA
- ⁴⁵ Department of Physics, University of Hong Kong, Pokfulam, Hong Kong
- ⁴⁶ Department of Astronomy and Astrophysics, Pennsylvania State University, University Park, PA 16801, USA
- ⁴⁷ Université Grenoble Alpes, CNRS, IPAG, 38000 Grenoble, France
- ⁴⁸ Center for Astrophysics, Harvard & Smithsonian, 60 Garden St, Cambridge, MA 02138, USA
- ⁴⁹ INAF Osservatorio Astronomico di Brera, via E. Bianchi 46, 23807 Merate (LC), Italy
- ⁵⁰ Mullard Space Science Laboratory, University College London, Holmbury St Mary, Dorking, Surrey RH5 6NT, UK
- ⁵¹ Anton Pannekoek Institute for Astronomy & GRAPPA, University of Amsterdam, Science Park 904, 1098 XH Amsterdam, The Netherlands
- ⁵² Guangxi Key Laboratory for Relativistic Astrophysics, School of Physical Science and Technology, Guangxi University, Nanning 530004, China